Master's Thesis

Fano Metamaterials on Nanopedestals for Plasmon Enhanced Infrared Spectroscopy

Jung. Yongseok

Department of Electrical Engineering

Graduate School of UNIST

2020

Fano Metamaterials on Nanopedestals for Plasmon Enhanced Infrared Spectroscopy

Jung. Yongseok

Department of Electrical Engineering

Graduate School of UNIST

Fano Metamaterials on Nanopedestals for Plasmon Enhanced Infrared Spectroscopy

A thesis/dissertation
submitted to the Graduate School of UNIST
in partial fulfillment of the
requirements for the degree of
Master of Science

Jung. Yongseok

12/02/2019 of submission

Approved by

Advisor
Jongwon Lee

Fano Metamaterials on Nanopedestals for Plasmon Enhanced Infrared Spectroscopy

Jung. Yongseok

This certifies that the thesis/dissertation of Jung. Yongseok is approved.

12/02/2019 of submission

signature

Advisor: Jongwon Lee

signature

typed name: Jooyun Jung

signature

typed name: Jiwon Chang

Abstract

Engineered optical metamaterials get attention to ultrasensitive analysis of biomolecules and gases materials owing to coupling effect between metamaterials and molecules in nanometer scale. The specific asymmetric structure supports a sharp and nonradiative Fano resonance exhibiting strong electromagnetic field enhancement and increased effective sensing area. Experimentally sample was fabricated with 2-cases that is the nanopedestal structure and the control structure for checking undercut effect in the molecular detection. For experimental demonstration of monolayer detection, ODT was chosen as a target molecule. Asymmetric nanorods are designed to have Fano resonance near the ODT fingerprint absorption wavelength. For experimental measurement, the ODT monolayer is coated on the fabricated sample and the reflection spectrum of the ODT coated sample is measured using a FT-IR spectrometer. Signal enhancement was confirmed owing to the increase in the sensing area and enhanced field enhancement at nanopedestal structure. The ODT signal result spectrum was modeled through TCMT to quantify amount of signal enhancement.

Contents

I. Background - - -

LIST OF FIGURES

LIST OF TABLES

Nomenclature

SPP	Surface Plasmon Polaritons
LSP	Localized Surface Plasmon
FT-IR	Fourier Transform Infrared
SEIRA	Surface Enhanced IR Absorption
FDTD	Finite-Difference Time-Domain method
PML	perfectly matched layer
NIL	nanoimprint Lithography
EBL	electron beam lithography
RIE	reactive ion etching
PUA	polyurethane-acrylate
MCT	Mercury Cadmiumtelluride
AsLSS	asymmetric least-squares smoothing
TCMT	Temporal coupled mode theory

I. Background

1.1 Plasmonic metamaterial

Plasmonic metamaterial is artificial materials engineered to have properties that have not yet been found in nature. Especially, it uses the collective electron oscillation behavior of free electrons in metal. The first metamaterial was researched by the 1898 Jagadis Chunder Bose using a twisted structure in the microwave range. Since then, metamaterial has been studied extensively around the world. Metamaterial interacts with electric and magnetic moment in the nanoscale unit and affects effective permittivity and permeability[1]. There are various parameters which are the size, shape and composition of the structure, density, orientation, and alignment, which can specify a electromagnetic response. These variables play an important role in the ultimate electromagnetic response characteristics.

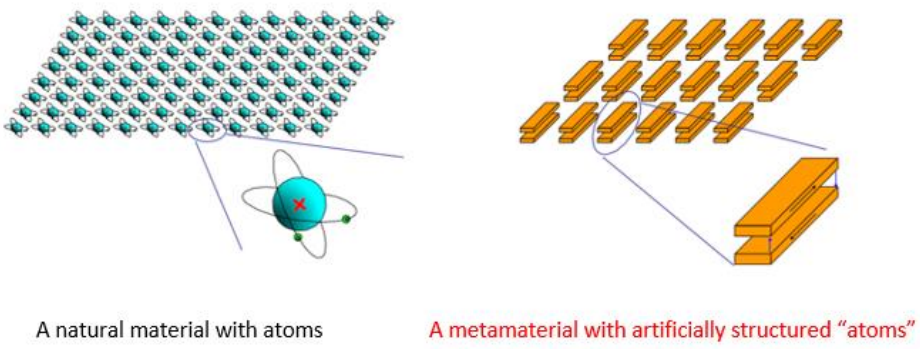

Figure 1-1. Schematic of Metamaterials characteristic[2]

Plasmonics is a phenomenon which electrons oscillate collectively under certain conditions in metal materials. It is a branch of nanophotonics and studied as surface plasmon. There are two types of plasmonics which is Surface Plasmon Polaritons (SPP)[3-5] and Localized Surface Plasmon (LSP)[5-8].

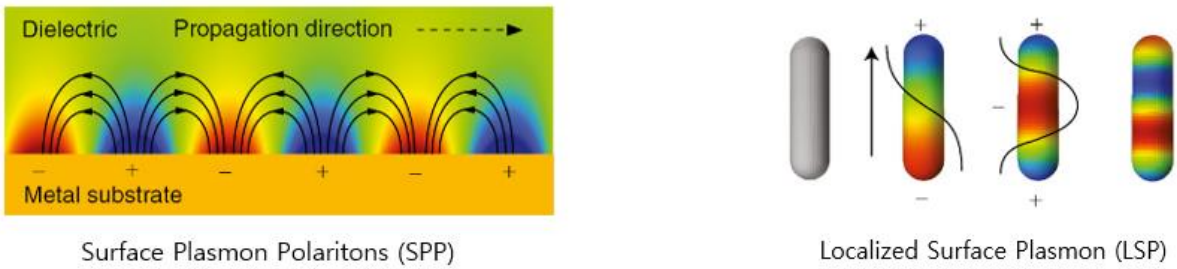

Figure 1-2. Plasmonic : Surface Plasmon Polaritons (SPP), Localized Surface Plasmon (LSP)

SPP can be generated in the infinite flat metal-dielectric region. It can be calculated by Maxwell's equations and boundary conditions.

$$z > 0$$
$$\overrightarrow{H_d} = (0, H_{yd}, 0)e^{i(k_{xd}x + k_{zd}z - \omega t)}$$
$$\overrightarrow{E_d} = (E_{xd}, 0, E_{zd})e^{i(k_{xd}x + k_{zd}z - \omega t)}$$

$$z < 0$$
$$\overrightarrow{H_m} = (0, H_{ym}, 0)e^{i(k_{xm}x + k_{zm}z - \omega t)}$$
$$\overrightarrow{E_m} = (E_{xm}, 0, E_{zm})e^{i(k_{xm}x + k_{zm}z - \omega t)}$$

$$\nabla \times \overrightarrow{H_i} = \varepsilon_i \frac{\partial \overrightarrow{E_i}}{\partial t}$$
$$i = d, m$$

, where ε_m is metal's permittivity, ε_d is dielectric's permittivity.

Applying the boundary condition as follows,

$$\varepsilon_m E_{zm} = \varepsilon_d E_{zd}$$
$$E_{xm} = E_{xd}$$
$$H_{ym} = H_{yd}$$

$$k_x = \frac{\omega}{c}\sqrt{\frac{\varepsilon_m \varepsilon_d}{\varepsilon_m + \varepsilon_d}}$$

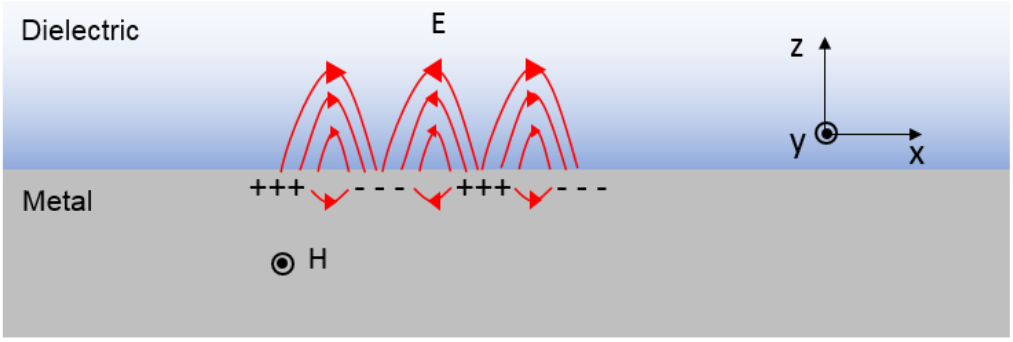

Figure 1-3. Schematic view of SPP between dielectric and metal

If ε_m becomes $-\varepsilon_d$, theoretically k_x becomes ∞, maximizing the sub-wavelength effect.

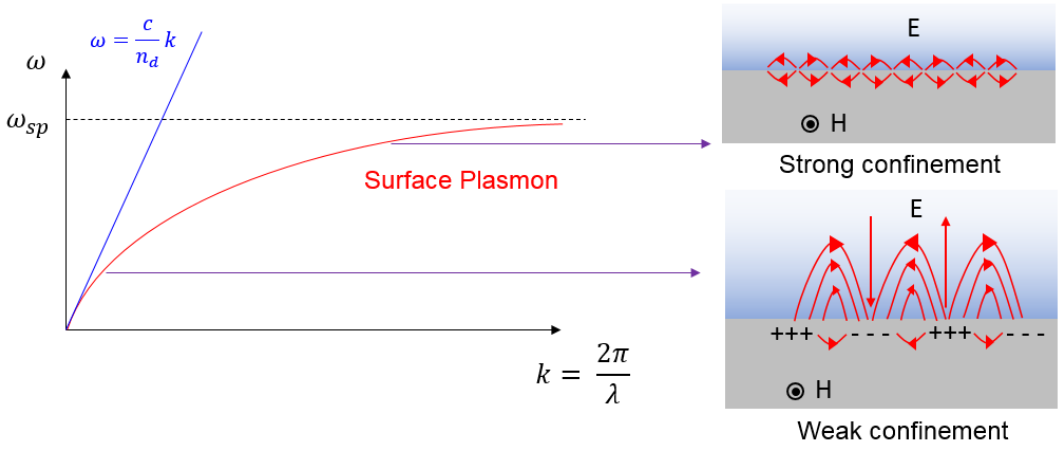

Figure 1-4. SPP's light confinement effect

On the other hand, LSP appears in nanoparticles rather than in infinite planar spaces. Because nanoparticles induced electric field can be approximated to dipole the polarizability is expressed as follows by the Clausius - Mossotti relation.

$$\alpha = \varepsilon_0 4\pi r^3 \frac{\varepsilon_d - \varepsilon_m}{\varepsilon_d + 2\varepsilon_m}$$

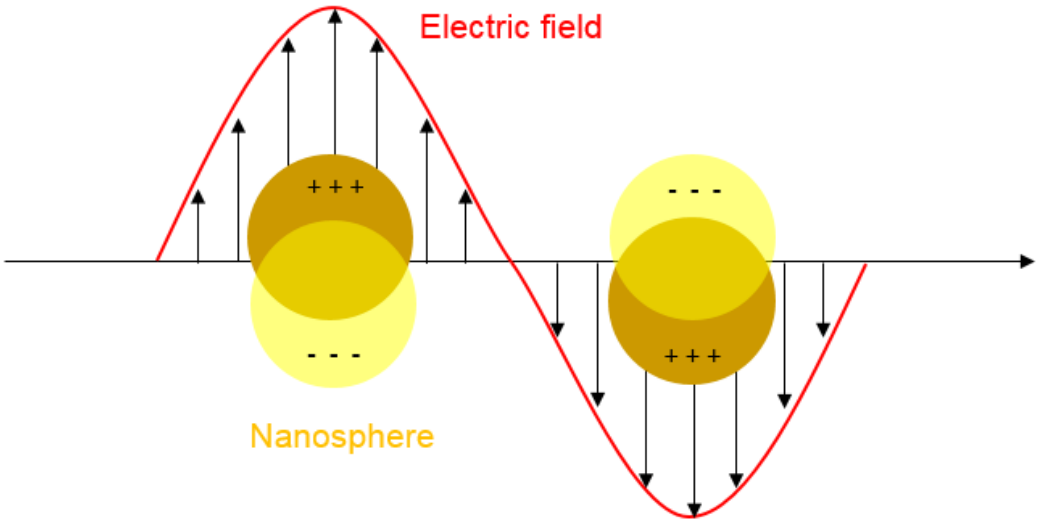

Figure 1-5. Illustration of LSP in which nanosphere is described as a dipole

Plasmonics can be applied to subwavelength optical devices[9-12], metamaterials & metasurfaces[13-17], high-resolution imaging[13,16-20], and biochemical sensing[21-24].

Figure 1-6. Applications of plasmonics[12,15-17]

1.2 SEIRA

Recently, label-free biomolecule detection is increasingly needed due to the development of bio industry. Especially, mid-infrared and THz region is very advantageous for detecting the material properties. Many of that region's materials have a unique vibration frequency[25]. Therefore, the substance can be detected reliably without sample's destructive manipulation[26]. Until now, Fourier transform infrared spectroscopy (FT-IR) equipment has been actively used for food detection and chemical detection.

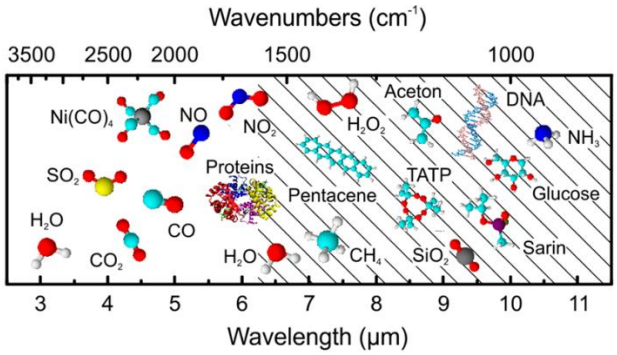

Figure 1-7. Characteristic of molecular vibration frequency[26]

However, because most of biomaterials' amounts are very small, it is difficult to detect with conventional FT-IR. To overcome this limitation, Plasmonic Surface Enhanced IR Absorption (SEIRA) spectroscopy is used by resonant coupling between surface plasmon resonance and molecular vibration. Thus, the nearby molecular vibration of this plasmonic resonance can be greatly enhanced through coupling. As shown in the figure below, the simple extinction of the molecular vibration (blue line) is very small. However, when combined with the near field enhancement of plasmonic resonance, the degree of molecular vibration becomes large. Therefore, even minute molecules can be detected.

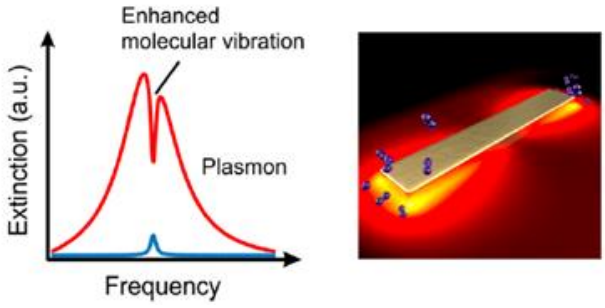

Figure 1-8. Extinction enhance by using of plasmonic near field enhance with molecular[26]

By using of quantum mechanical, asymmetric line appears which is discovered by Ugo Fano[28]. Fano resonance asymmetric structure characteristic has many advantages in comparing with other SEIRA structure[29-31]. It has sensitive spectrum with high quality factors and strong field enhancement. That is, it is optimized for ultrasensitive detection. In 2011, Wu et al examined biosensor by using of asymmetric gold rods[32].

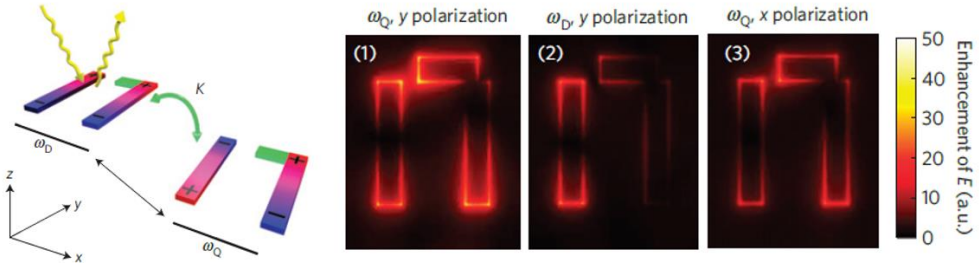

Figure 1-9. Schematic view of Fano structure for protein detection[32]

In general, nevertheless, the general SEIRA structure consists of a two-dimensional planar structure. However, because the large near field is mostly present in the metal structure, the molecular vibration can't be maximally enhanced[33]. So, with the pedestal structure, additional access can be used for sensing method which is the bottom surface.

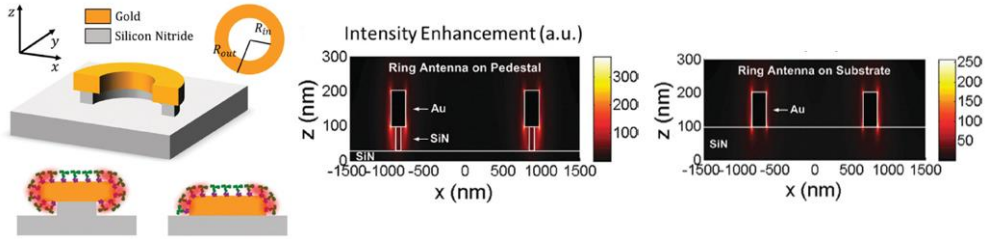

Figure 1-10. SEIRA structure – antennas on pedestals[33]

1.3 Fano Resonance

Quadrupole resonance and dipole resonance exist in Fano Resonance. In the figure below, there is a metal rod parallel to the *y*-axis. And there is a short rod on the right rod parallel to the x axis in green. This is called asymmetric factor because it breaks the symmetrical structure. If this asymmetric factor is present, the quadrupole resonance as well as the dipole resonance will appear by the *y* polarized incident light. If this asymmetric factor does not exist, there is only a normal symmetric rod. This structure will only show normal Lorentzian type dipole resonance. In a simple symmetric structure, the sub-radiant mode is perfectly dark. In other words, sub-radiant mode (= quadrupole resonance) appears by the asymmetric factor. This is because the sub-radiant mode (= quadrupole resonance) is directly coupled with the super-radiant mode (= dipole resonance). Thus, the spectrum becomes asymmetric non-Lorentzian form. Here, sub-radiant mode is called dark mode and super-radiant mode is called bright mode. Meanwhile, the dipole resonance frequency exists in $\omega_D \approx 2000cm^{-1}$ as shown below, and the quadrupole resonance frequency exists in $\omega_Q \approx 1500cm^{-1}$ by *x*-polarized incident light result.

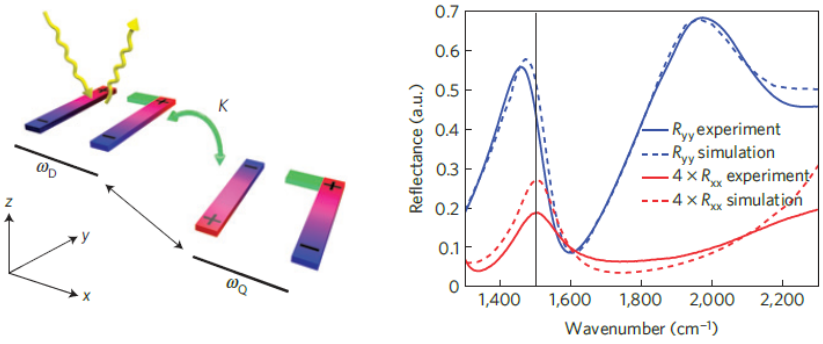

Figure 1-11. Electromagnetic properties of Fano metamaterials and experiment and simulation result[32]

In the *y*-polarized result where the typical Fano shape appears, a strong field enhancement appears at the quadrupole resonance frequency point. As shown in the figure below, the field enhancement is the largest at quadrupole resonance frequency of *y*-polarized incident light (1).

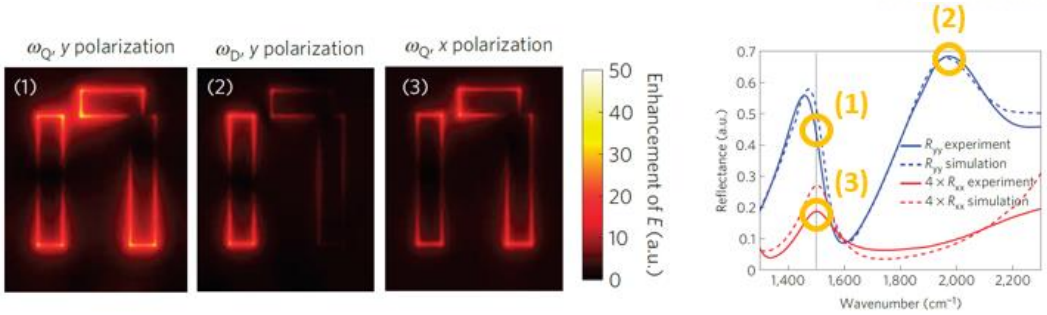

Figure 1-12. Field enhancement at y polarization ω_Q, ω_D and x polarization ω_Q[32]

II. Structure Design & Simulation

2.1 FDTD Simulation

Finite-Difference Time-Domain method (FDTD) basically utilizes Maxwell's equations with numerical analysis. That is, each component is discretized and calculated in the form of gird. High temporal and space resolution can be applied to obtain accurate values. However, in this case, the calculation data will exponentially increase, so other algorithms are needed. Most of commercial FDTD basically operates as a Yee-algorithm[34]. As shown in the figure, the components of each vectors are located at i, j, and k, respectively. This automatically meets divergence conditions and automatically meets interface conditions. That is, the FDTD calculation can be simplified. Numerical calculations were performed using Lumerical Solutions, ver.8.19.

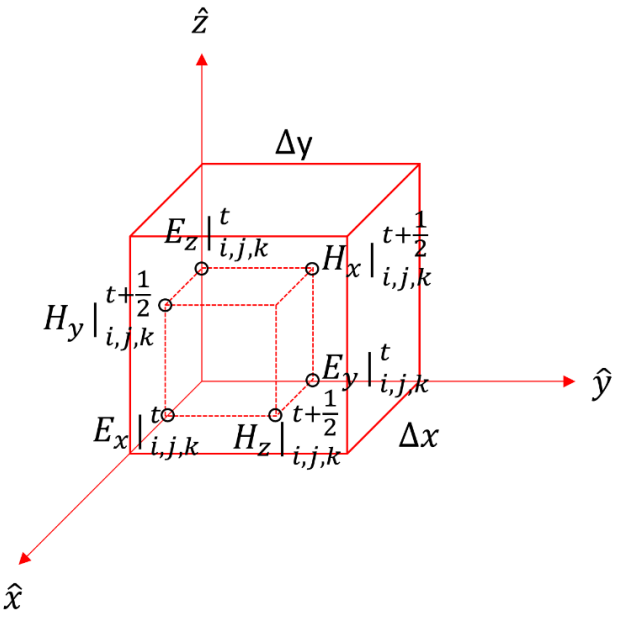

Figure 2-1. Method of Kane Yee algorithm grid algorithm

$$\nabla \times \boldsymbol{E} = -\mu \frac{\partial \boldsymbol{H}}{\partial t} \quad \textit{Faraday's law}$$

$$\boldsymbol{H}|^{t+\frac{1}{2}} = \boldsymbol{H}|^{t-\frac{1}{2}} - \Delta t \mu^{-1} \nabla \times \boldsymbol{E}|^{t} \quad 2$$

$$\nabla \times \boldsymbol{H} = \varepsilon \frac{\partial \boldsymbol{E}}{\partial t} \quad \textit{Ampere's law}$$

$$\boldsymbol{E}|^{t+1} = \boldsymbol{E}|^{t} - \Delta t \varepsilon^{-1} \nabla \times \boldsymbol{H}|^{t+\frac{1}{2}} \quad 4$$

The reason of fundamental difference between semiconductors, insulators and conductors is due to differences in energy band structure. Each of the atomic materials has a unique orbital. Electrons in the outermost shell can't generate an electrical current. When an electron escapes from the nucleus, or exits the outermost shell, the electrons become free electrons and generate an electrical current. And, When many atoms are bonded to form a solid, the orbits of electrons overlap, the orbit is called a band. The conduction band of a conductor, such as most metals, overlaps the valence band and has a very low band gap energy. Due to the low band gap energy, electrons can be excited across the band gap even at room temperature. Therefore, there are many electrons in the conduction band, and electric conduction easily occurs by these electrons.

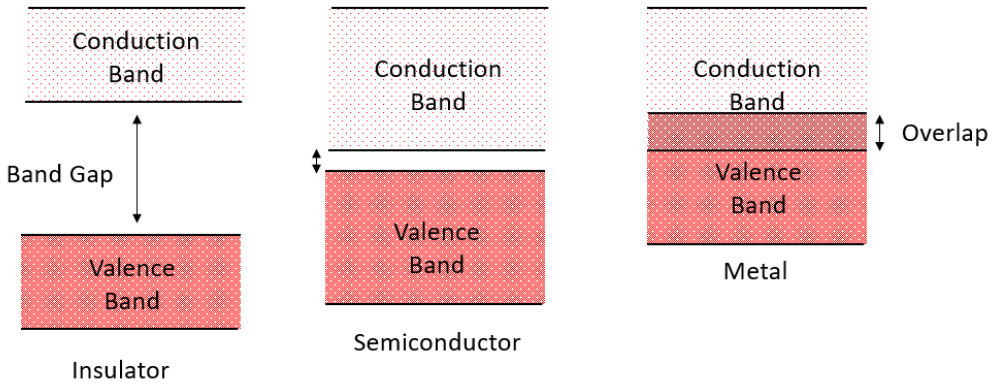

Figure 2-2. Energy band diagram of insulator, semiconductor and metal

Drude model is a good explanation of the properties of metal materials. It is assumed that the free electrons in the conductor move infinitely.

$$\varepsilon(\omega) = 1 - \frac{\omega_p^2}{\omega^2 + j\gamma\omega}$$

$$\omega_p^2 = \frac{ne^2}{\varepsilon_0 m_e}$$

If considered by the region from which electrons have escaped,

$$\varepsilon_\infty - \frac{\omega_p^2}{\omega^2 + j\gamma\omega}$$

Where γ represents damping frequency. And, ω_p means plasma frequency, which is related to electron density. Below the plasma frequency, the dielectric constant becomes negative as shown below. This region is called the metal region.

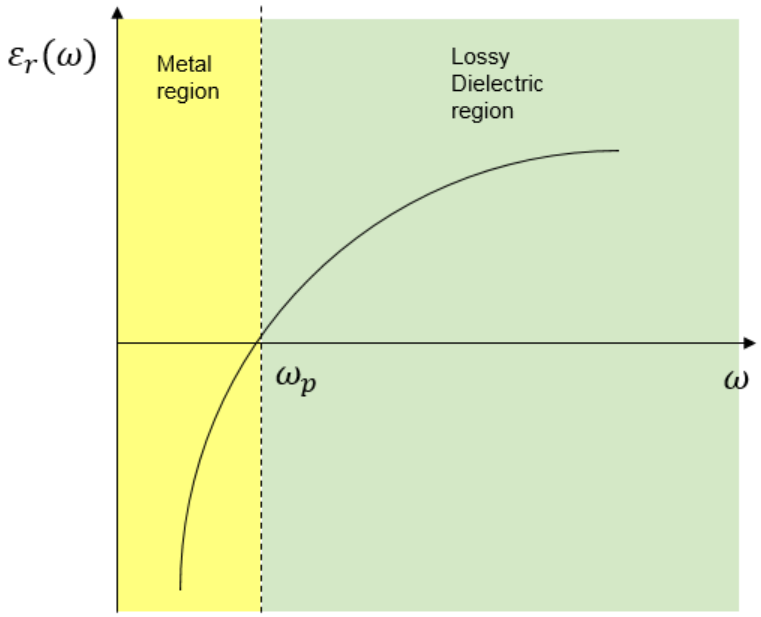

Figure 2-3. Lossless Drude model for metal region

2.2 Parameter Model, Simulation Setting

In this simulation, Drude model was used with the collision frequency $\gamma = 1.224 \times 10^{14}$ rad/s and the plasma frequency $\omega_p = 1.37 \times 10^{16}$ rad/s. And, Quartz was modeled with SiO_2 (Glass) Palik, which is basically set in the Lumerical. Structure was made like the figure. In addition, Lumerical was set to the boundary condition as x and y as periodic and the z boundary as a Perfectly Matched Layer (PML). In the case of undercut, it was assumed to be isotropic etching. That is, as shown in the figure, $\Delta x = \Delta y = \Delta z$. *X*-polarization and *y*-polarization result was confirmed by using s-params. The mesh was set to 3.

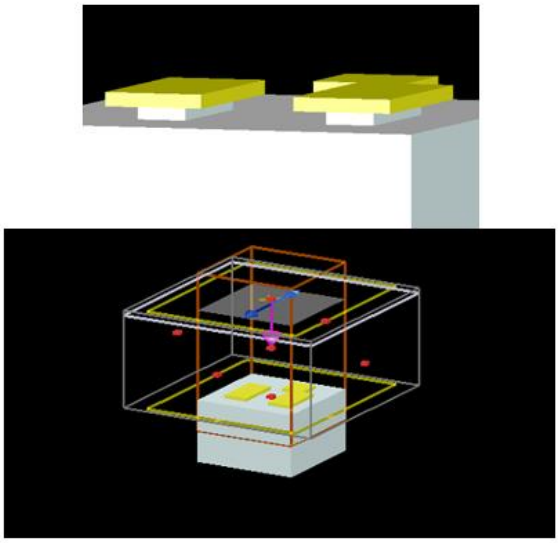

Figure 2-4. Lumerical Simulation example for Fano structure

III. Fabrication Processing

3.1 Fabrication Step

Fano Structure was created using the nanoimprint lithography (NIL) method. In the fabrication, sample was made by 1.7μm periodic array with a size of 700μm x 700μm in the NIL.

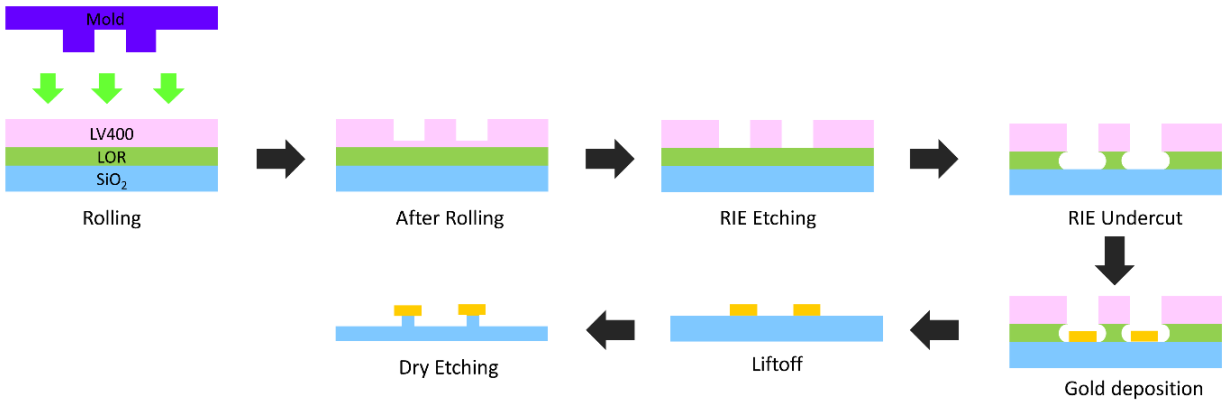

Figure 3-1. Nanoimprint lithography

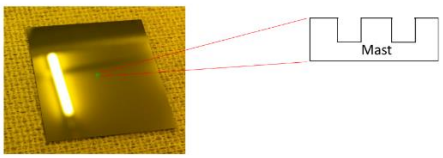	The first step of nanoimprint was mast production. Mast was designed by a CAD program. The desired shape was fabricated on the Si substrate using electron beam lithography (EBL) and reactive ion etching (RIE) equipment.
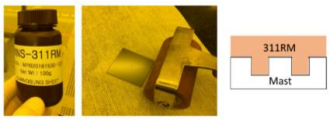	Then, mast was dropped by the UV resin 311RM solution by 2 ~ 3 drops and covered the polyurethane-acrylate (PUA) mold film and roll.
	Then, in this state, the UV illuminator cured for 90 sec. Similarly, this combined sample was detached and mold film were putted to UV illuminator for 90sec. Then, when the mast was separated from the mold film, the desired pattern was transferred to the mold film as shown in the figure.

	Meanwhile, the SiO_2 substrate was further deposited with an electron beam evaporator to 100nm of SiO_2. This was to make the nanopedestal structure through the undercut process at the last process. It was cleaned by the Asher equipment for 60sec to improve the surface adhesion.
	Then, a syringe was used on the wafer by the LOR 1A uniformly so that no bubbles were formed. Spin coating was then carried out at 4000rpm for 60sec.
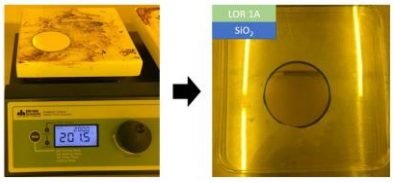	LOR coated SiO_2 wafer was cured on the hot plate for 30min at 200°. Then, it was cooled down on the steel plate for 15min.
	The coated LOR was then cleaned again in Asher for 60sec to improve adhesion.
	Next, the LV 400 solution (1cc) was dropped on the LOR coated SiO_2 so that no air bubbles were formed. The spin coating was then run at 2000rpm for 60sec.
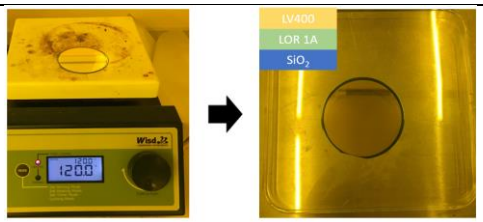	The SiO_2 wafer coated to LV400 was cured at 120°C for 40sec on the hot plate. Cool down was not done after this.
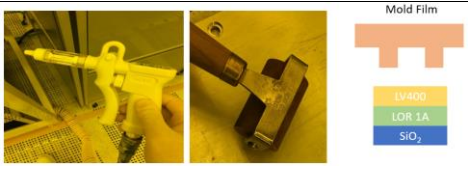	N_2 blowing was performed to remove unwanted particles on the SiO_2 wafer surface, and the mold film was covered and rolled on SiO_2 wafer.

	Then compressor was used to mold the pattern on the LV 400. At this time, sample was covered with vinyl before compression. It was set by the pressure to 3bar and proceeded for 5min. Finally, it was set by the UV time for 95sec to allow the LV 400 to cure well.
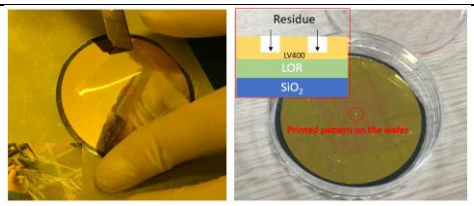	The pattern was observed when the film was removed with a cutter knife with residue on the LV400 as shown in the figure.
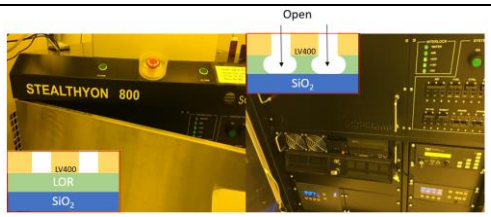	CF_4 and O_2 gas conditions at 100W were used to remove LV 400 residues. The LOR layer was undercut to vertically deposit Gold on SiO_2. At this time, O_2 gas condition was used as 50W in RIE.
	To progress the gold depositions, first Au and Ti were contained in the crucible. Ti was used to improve adhesion between SiO_2 and Gold. And sample was placed in the load lock chamber of the E-beam evaporator. And it was kept in high vacuum for 100min. Finally, Ti 3-4 nm was deposited and Au was 100nm thickness.
	Finally, the wafer was cleaned with acetone IPA and then immersed in LOR etchant solution to lift off LOR 1A.
 	And, to make the nanopedestal structure, O_2 30sccm CF_4 15sccm with 300W condition was applied to Asher equipment for 1 min.

Table 3-1. Picture of fabrication step

IV. Experiment Result

4.1 Measuring & Experimental Equipment

<table>
<tr>
<td> 
FT-IR Spectroscopy (Bruker, Spectrometer Vertex 70)</td>
<td> 
Lock in amplifier (AMTEK 7265)</td>
</tr>
<tr>
<td> 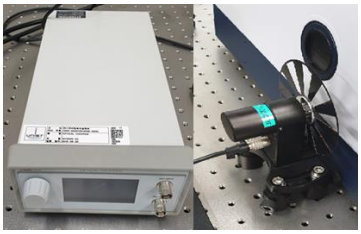
OPTICAL CHOPPER (MC2000-EC)</td>
<td> 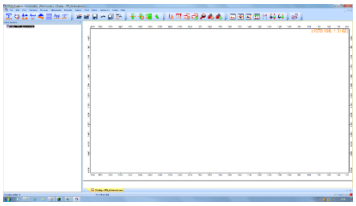
OPUS Software(7.5 Build: 7, 5, 18 (20140810))</td>
</tr>
<tr>
<td> 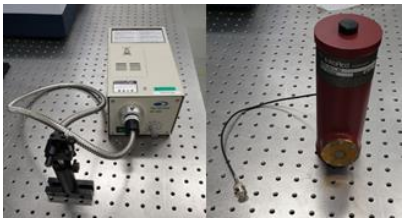
Illuminator (FOK-100W) and A liquid nitrogen cooled Mercury Cadmiumtelluride (MCT) Infrared detector (MCT-16-1.00)</td>
<td rowspan="2"> 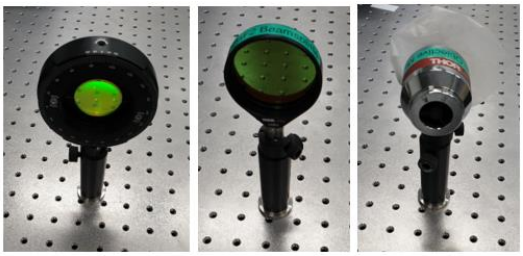
Rotatable holographic wire grid polarizer (ZnSe, THORLABS), CaF_2 Beam splitter (Thorlabs), Objective lens (Thorlabs)</td>
</tr>
<tr>
<td> 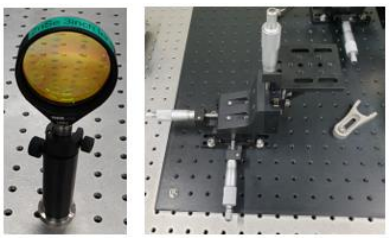
ZnSe 3inch lens (Thorlabs) and 3D stage (NAMIL ATS4P)</td>
</tr>
</table>

Table 4-1. Picture of measuring and experimental equipment

4.2 Experiment Step

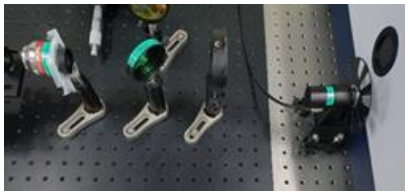	First, the MCT Detector was filled with LN2 as shown. Next, chopper, wire grid polarizer, ZnSe Polarizer, and Objective lens was installed in a line as shown in the figure.
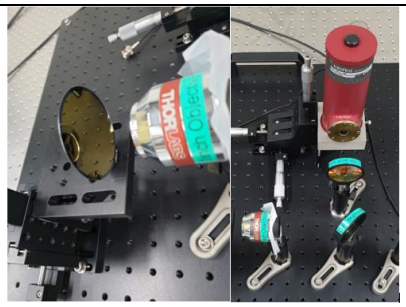	Then, in the direction of the objective lens, the Gold background on the 3D stage was mounted as follows. On the opposite side of the Beam Splitter, a 3-inch ZnSe lens and a detector was installed as shown.
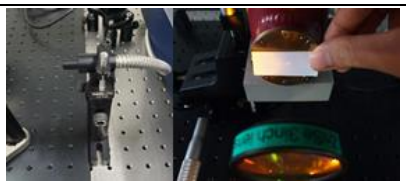	Then the Illuminator was installed on the front to align. And the Illuminator was used to adjust the beam splitter angle and the focus distance of the 3D stage to come to the center of the MCT detection.
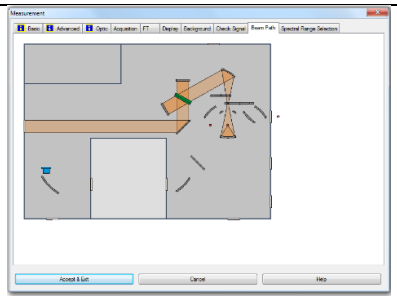	Then, Beam path was set in the OPUS program as follows.
	The sample was adjusted to the z direction of the 3D stage as shown in the figure. At the same time, the 3D stage of the MCT detector was adjusted to focus on the center by adjusting x, y. After focusing, it was set to the resolution 2cm^{-1} and sample scan time 64 as follows to measure the background to be normalized.
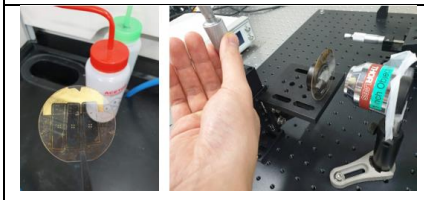	The sample to be measured was first cleaned with acetone and IPA to remove organic solvents. Then it was mounted in the 3D stage to focus on x and y. In OPUS program, spectrum was normalized by background signal and sample signal.

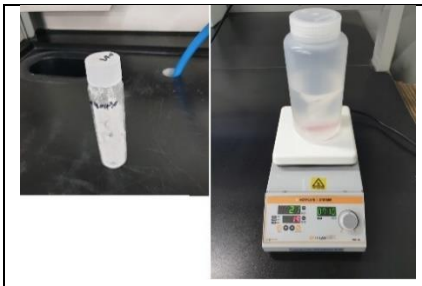	Meanwhile, 0.144g of ODT powder was added to 500 ml of ethanol to adjust 1moles of ODT, and the solution was mixed with a magnetic bar for 24 hours using a stirrer.
	The sample was immersed in the ODT solution for 24h as shown in the figure.
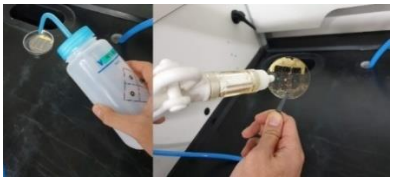	Then to measure the ODT monolayer, the ODT coated sample was again immersed in a pure ethanol solution for 30 minutes and subjected to N2 blowing. Sample was mounted on the 3D stage and focused on x and y. In OPUS program, sample was normalized by background signal and sample signal.

Table 4-2. Picture of experiment setup

The following is a schematic that is a simplified version of the actual installed optical table.

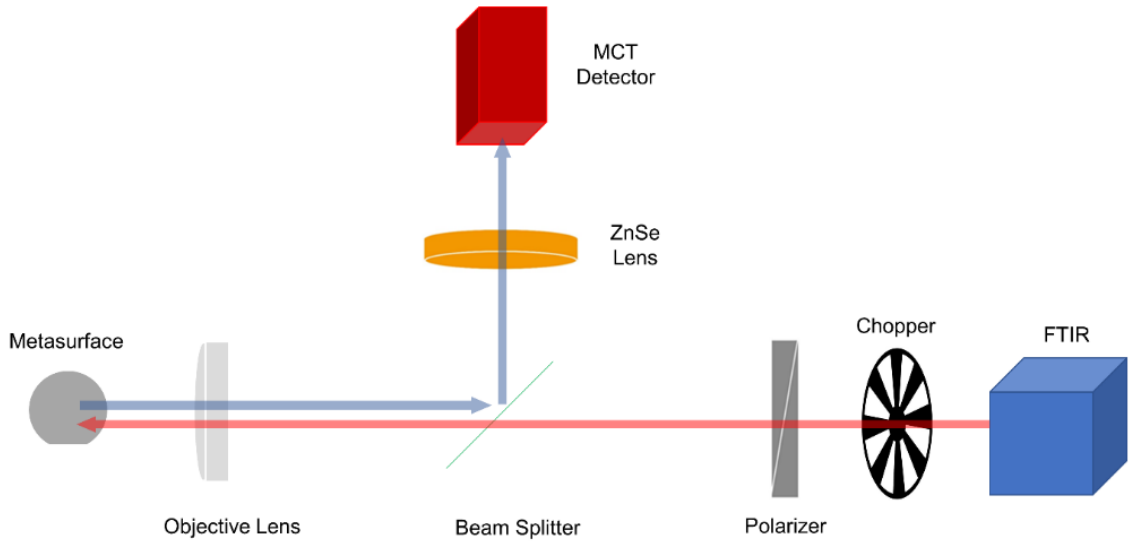

Figure 4-1. Schematic of measurement setup

4.3 Experiment Result

First the Fano structure was designed as follows. See 2.2 for various simulation parameters.

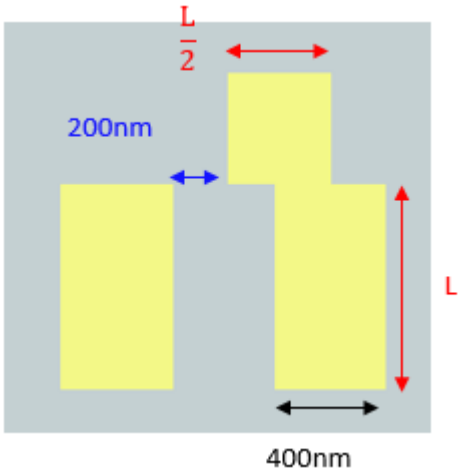

Figure 4-2. Schematic view of Fano structure unit cell

The width was fixed at 400nm and the rod bar gap was fixed at 200nm. Particularly, the reason for fixing to 200nm was because it was difficult to make the structure less than 200nm due to the limitation of resolution. Meanwhile, periodic was also fixed at 1700nm. The reason for this was that the Lumerical simulation was first optimized to the approximate ODT absorption frequency by the trial and error method. And length was adjusted to match the ODT absorption frequency exactly. First, *x*-polarization results were confirmed at L = 680nm, 740nm, and 800nm. As shown in the figure below, sample was first set to exactly 3.427μm at L = 680nm. Then, L = 740nm, 800nm was increased by red shift, which was for the undercut structure. In other words, when the undercut was performed, the effective refractive index was decreased and blue shift occurred.

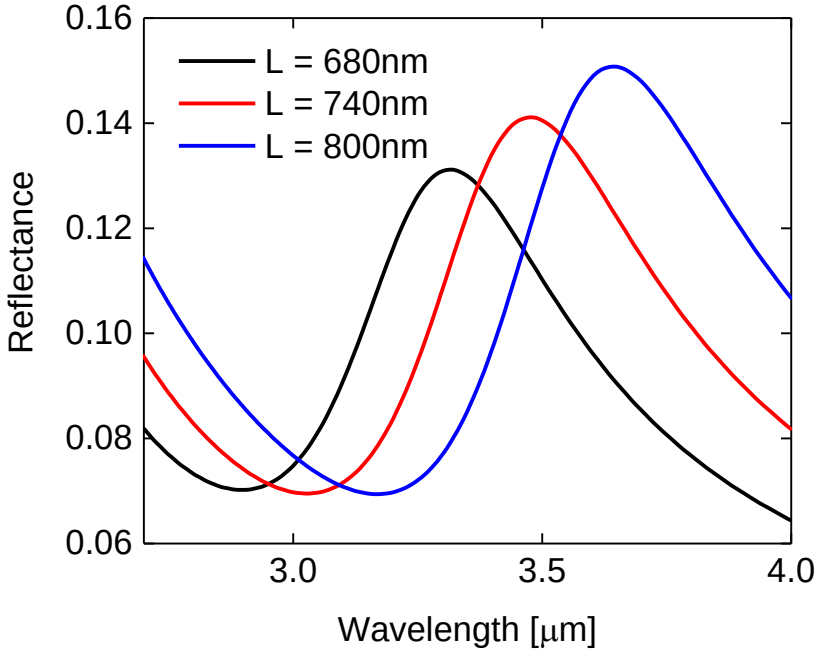

Figure 4-3. *x*-polarization simulation result

In the *y*-polarization result, dipole resonance frequency ω_D could be checked by peak value. And the quadrupole resonance frequency was confirmed in the *x*-polarization result. It was checked where the field enhancement was the greatest. That is, it was observed to field enhancement in ω_D and ω_Q at *y*-polarization and field enhancement in ω_Q in *x*-polarization.

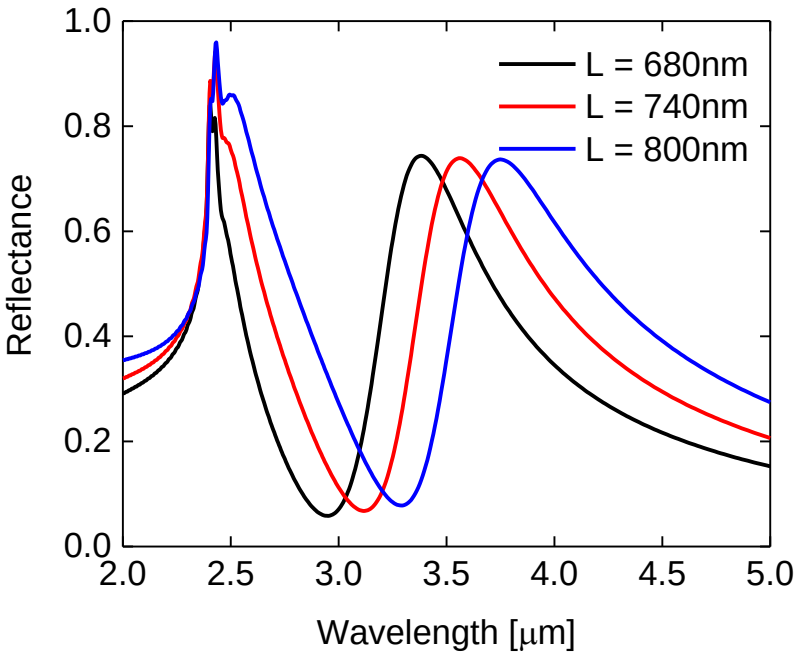

Figure 4-4. *y*-polarization simulation result

The field enhancement monitor dimension was set as the top part of the gold rods as shown in the figure. It was set to the override mesh to 4nm to improve the accuracy. Therefore, it was checked to the ω_Q, ω_D when it was *y*-polarization and ω_D when it was *x*-polarization, respectively, on the monitor.

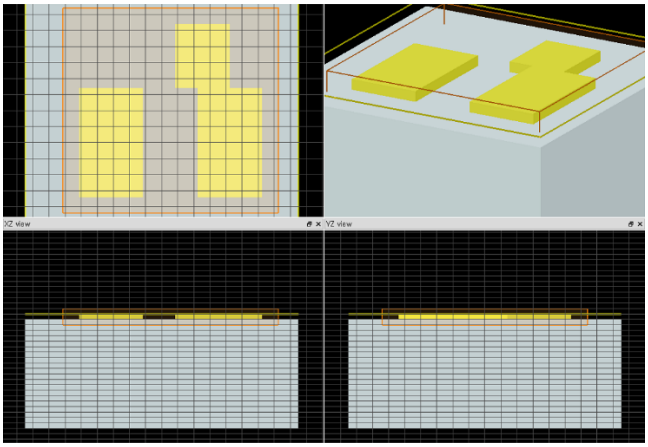

Figure 4-5. Field enhancement monitor and override mesh

The following figure shows the order of field enhancement in ω_Q and ω_D at *y*-polarization and field enhancement at ω_Q in *x*-polarization. As expected, field enhancement was the greatest in ω_Q at *y*-

polarization. Field enhancement in ω_D at *y*-polarization shows that field enhancement is greatest at both ends of the dipole rod bar, and observation of field enhancement at ω_Q in *x*-polarization shows field enhancement at both ends in the transverse direction.

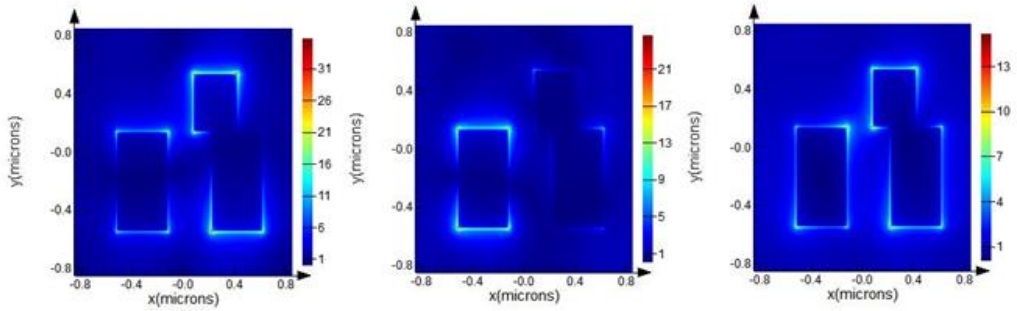

Figure 4-6. Field enhancement in ω_Q and ω_D in *y*-polarization and field enhancement in ω_Q in *x*-polarization

Meanwhile, it was checked how much the field enhancement is enhanced as the undercut is performed. As would be explained later, the 30nm isotropic undercut resulted in simulation were same as actual 1min Asher undercut. Interestingly, field enhancement in ω_D at *y*-polarization and field enhancement in ω_Q at *x*-polarization were nearly identical before and after undercut. However, field enhancement in ω_Q at *y*-polarization was increased further. Therefore, undercuts were expected to increase the ODT sensing capability due to the increase in field enhancement with the previously mentioned effective area increase.

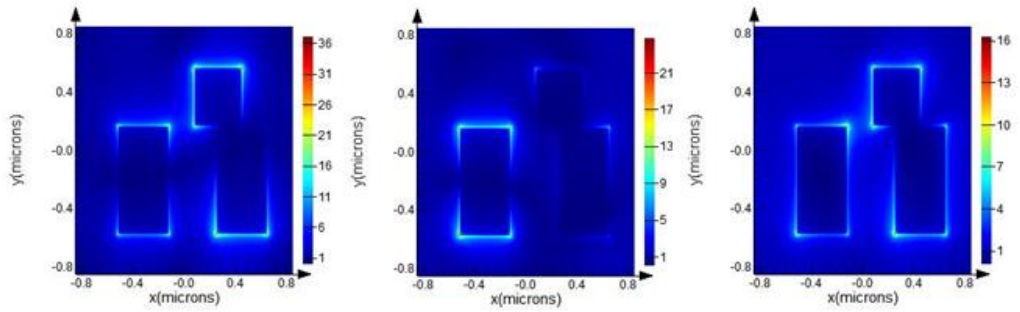

Figure 4-7. L = 740nm, 30nm isotropic undercut Field enhancement in ω_Q and ω_D in *y*-polarization and field enhancement in ω_Q in *x*-polarization

And the actual Fano structure wafer was measured. Interestingly, the simulation result and the actual

experiment result were almost identical.

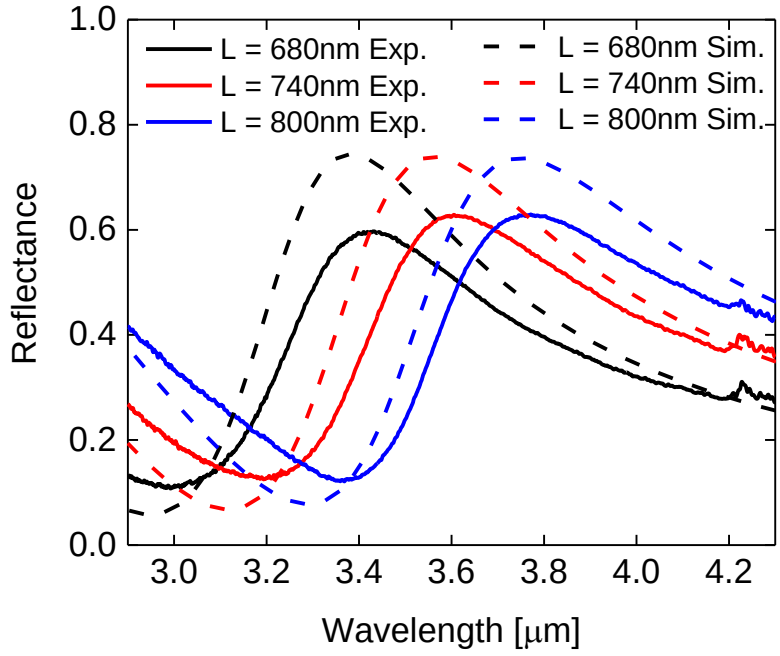

Figure 4-8. *y*-polarization experiment and simulation result with substrate structure

It was checked to *x*-polarization too. As with the *y*-polarization result, there was a good agreement.

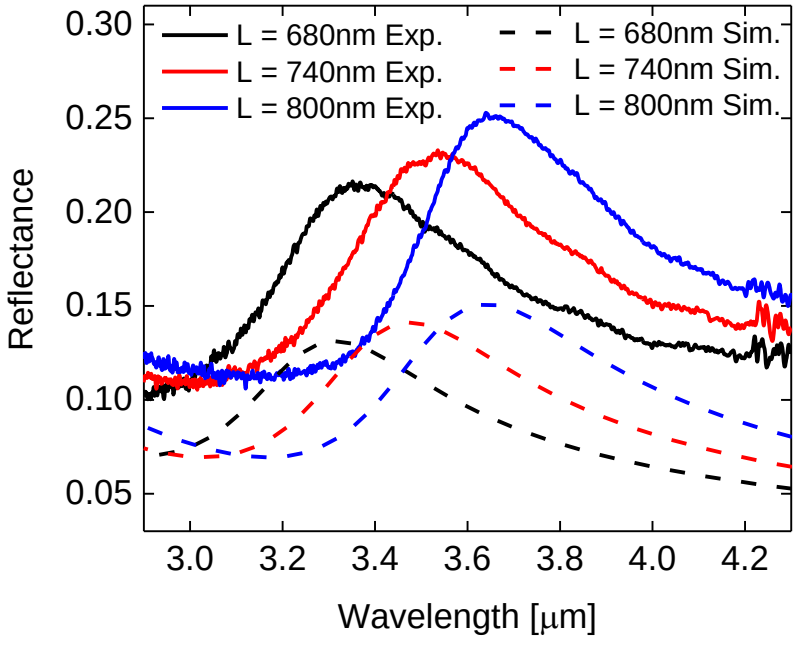

Figure 4-9. *x*-polarization experiment and simulation result with substrate structure

The following shows the *x*-, *y*- polarization results of the substrate structure simultaneously. There is a quadrupole resonance in the left shoulder at the peak position on the *y*-polarization basis. Therefore, the ODT signal was expected to be best observed when the ODT absorption frequency matches that frequency.

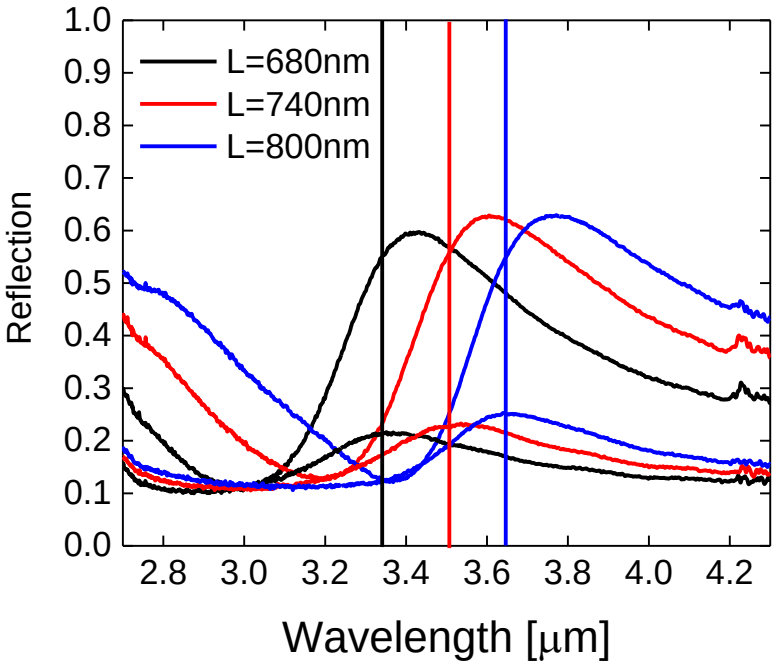

Figure 4-10. Simultaneous *x*, *y* - polarization result with substrate structure

Next, the Asher process (1min) was performed on the Fano structure wafer to make the nanopedestal structure. (See. Table 3-1 last step) Before and after the sample Asher process, A frequency shift was observed as expected. Blue shift was observed by approximately 0.18μm.

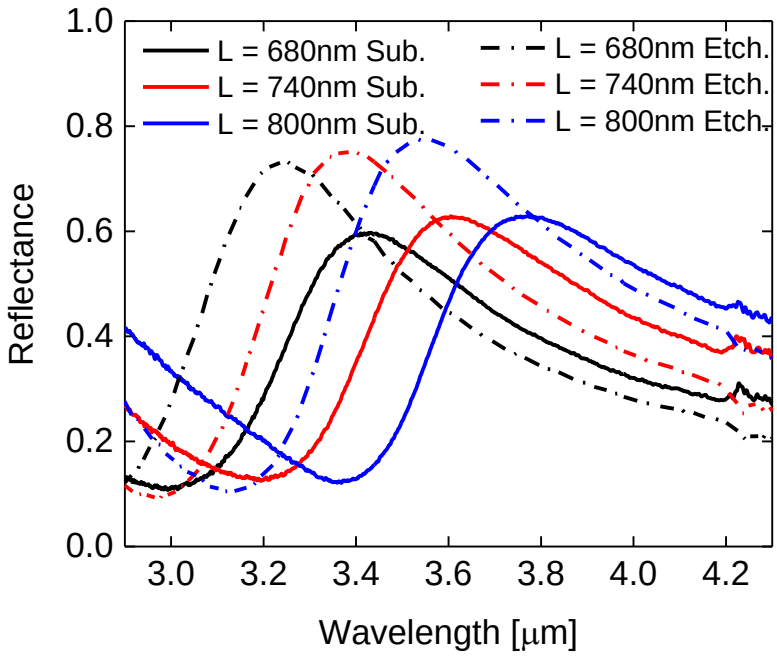

Figure 4-11. *y*-polarization experiment result with substrate and etch structure

Compared with the simulation, when the undercut of 30nm was performed, the spectrum agreed well.

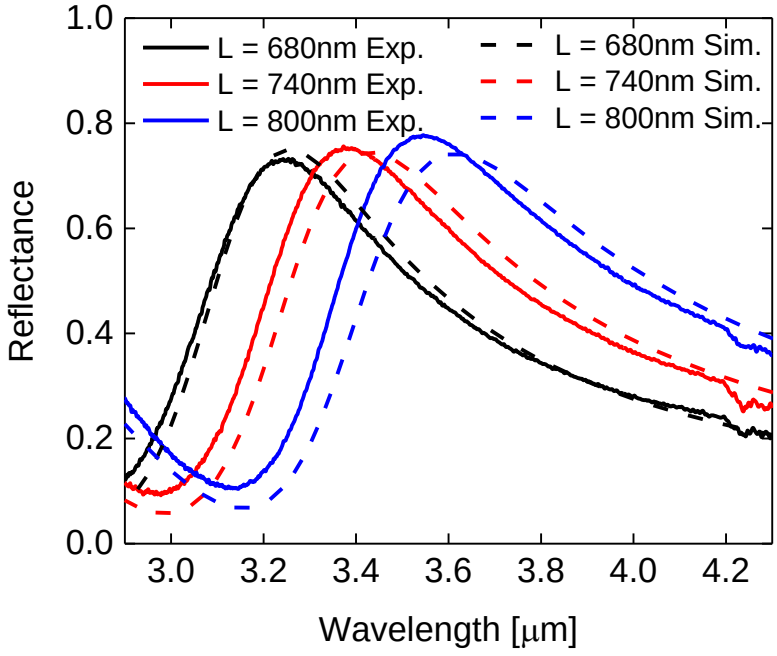

Figure 4-12. *y*-polarization experiment and simulation result with etch structure

Next, the ODT signal was checked with before and after Asher process (substrate structure and etch

structure). First, it was checked the substrate structure result. As expected, the ODT signal was the largest measured at L = 680nm, which most closely matches the quadrupole resonance. Others, L = 740nm and 800nm, signal distortion due to ODT molecule was very low.

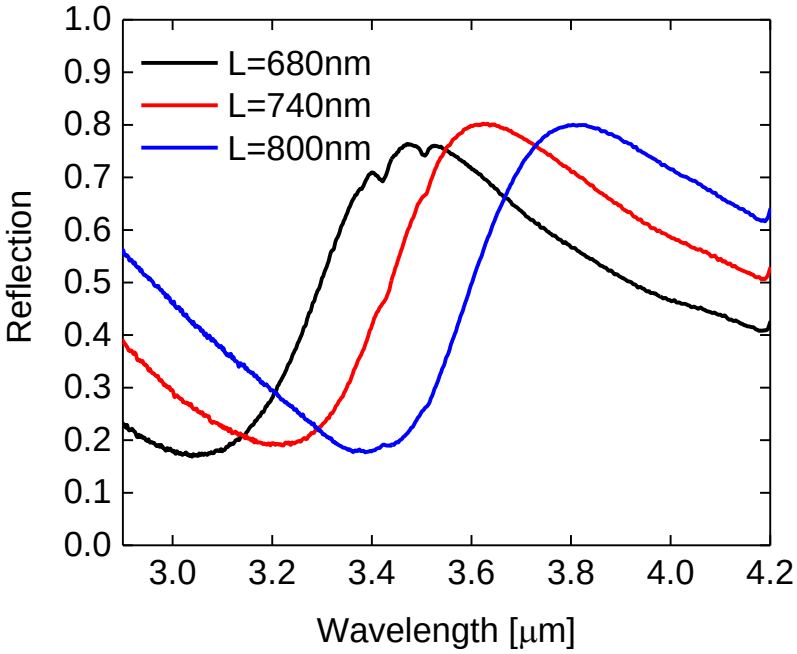

Figure 4-13. *y*-polarization experiment result with ODT coating with Substrate structure

And ODT signal was confirmed in etch structure. Overall, the ODT signal increased significantly due to the increase of the effective area. ODT signal was observed at L = 740nm, which is consistent with quadrupole resonance frequency and ODT absorption frequency.

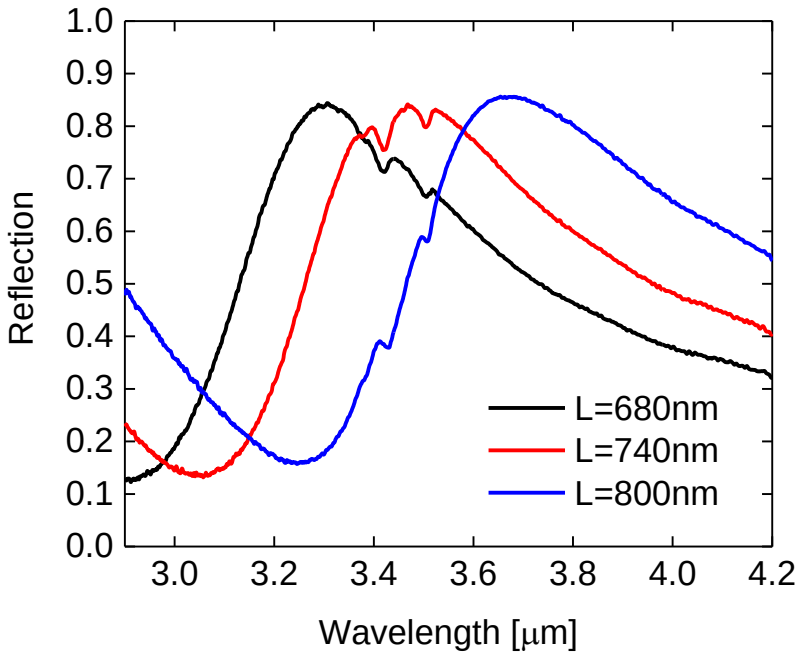

Figure 4-14. *y*-polarization experiment result with ODT coating with Etch structure

Next, the difference of reflectance was calculated for each sample through the asymmetric least-squares smoothing (AsLSS) algorithm. [Ref] That is, baseline was calculated through AsLSS and then calculated by $R_{Baseline} - R_{ODT}$. The red line is the result of the etch structure's $R_{Baseline} - R_{ODT}$ and the black line is the result of the substrate structure's $R_{Baseline} - R_{ODT}$. The largest ΔR in the substrate structure was L = 680nm. However, in the case of the etch structure, the smallest ΔR was larger than the ΔR at the substrate 680nm which is largest ΔR. In other words, it could be seen that the effect of increasing the effective area by undercut played a decisive role in sensing.

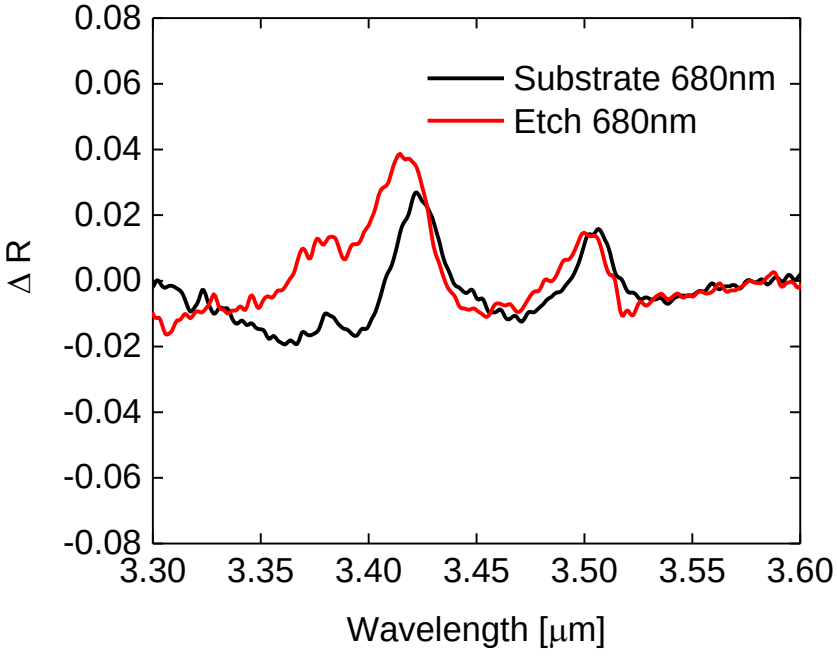

Figure 4-15. ΔR between L=680nm before substrate after etch structure

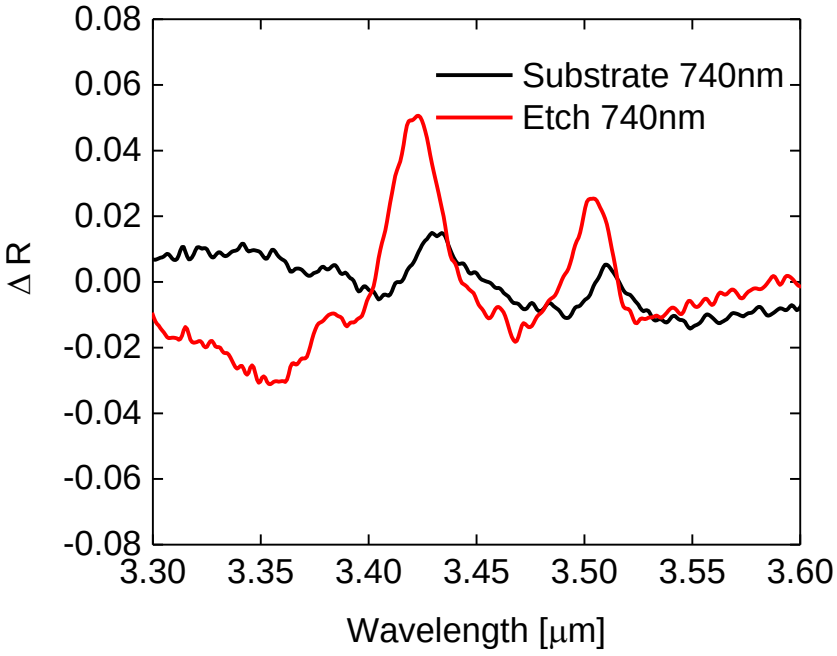

Figure 4-16. ΔR between L=740nm before substrate after etch structure

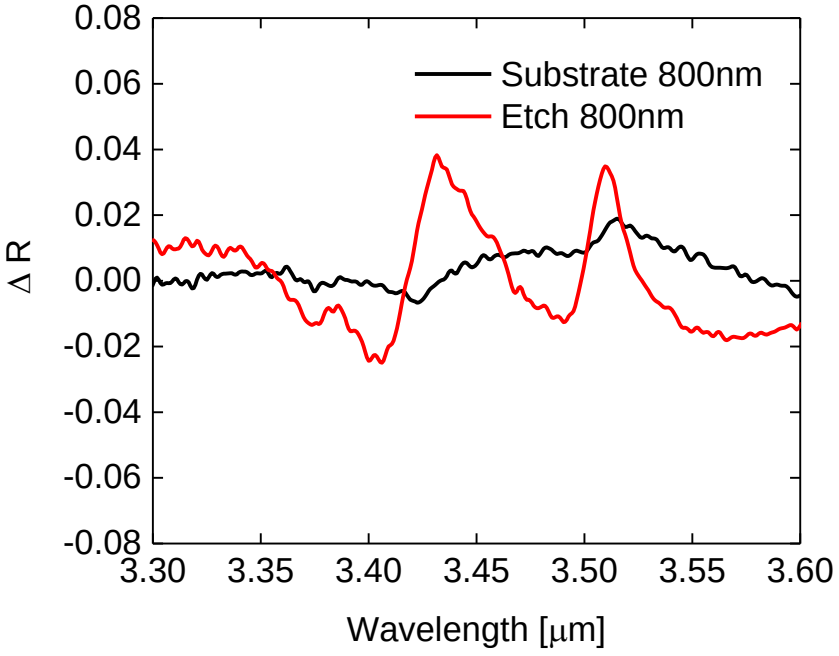

Figure 4-17. ΔR between L=800nm before substrate after etch structure

V. TCMT Modelling

5.1 Theory

Temporal coupled mode theory (TCMT) is an equation that expresses two states when they have two states like Fano structure. It can be expressed as follows[32,35].

$$\frac{dA_1}{dt} = j\omega_1 A_1 - \left(r_{1x} + r_{1y} + r_1^{Ohm} \right) A_1 + \kappa_{12} A_2 + \alpha_{1x} S_x^{in} + \alpha_{1y} S_y^{in}$$

$$\frac{dA_2}{dt} = j\omega_2 A_2 - \left(r_{2x} + r_{2y} + r_2^{Ohm} \right) A_2 + \kappa_{21} A_1 + \alpha_{2x} S_x^{in} + \alpha_{2y} S_y^{in}$$

There are two kinds of Eigenstate like A_1, A_2. x, y means that the incident light has two kinds of x- y-polarization. S_i (i = x, y) represents incident Power. That is, $|S_i|^2 = \frac{c\varepsilon_0}{2}|E_i|^2$. $|A_i|^2$ represents each stored energy. γ_i is the radiative damping rate, and r_i^{Ohm} is the ohmic damping rate. κ_{12} or κ_{21} indicates the coupling strength between each eigenstate. In the case of the Fano Structure used in our experiment, a symmetric break parameter is added.

$$\frac{dA_1}{dt} = j\omega_1 A_1 \; - \; \left(\; r_{1y} + \; r_1^{Ohm} \right) \; A_1 + \; \kappa_{12} A_2 + \; \alpha_{1y} S_y^{in}$$

$$\frac{dA_2}{dt} = j\omega_2 A_2 \; - \; \left(\; r_{2x} + \; r_{2y} + \; r_2^{Ohm} \; \right) \; A_2 + \; \kappa_{21} A_1 + \; \alpha_{2x}(L_2) S_x^{in} + \; \alpha_{2y} S_y^{in}$$

In the case of Dipole and Quadrupole mode in Fano Structure, Q = A_1 - A_2 and D = A_1 + A_2. Therefore, finally, it can be expressed as follows.

$$\frac{dD}{dt} = j\omega_D D - \tau_D^{-1} D + j\kappa Q + \alpha_{D_x} S_x^{in} + \alpha_{D_y} S_y^{in}$$

$$\frac{dQ}{dt} = j\omega_Q Q - \tau_Q^{-1} Q + j\kappa D + \alpha_{Q_x} S_x^{in}$$

As can be seen from the equation, in the case of the dipole parameter, both the *x*- polarization and the incident light of *y*- polarization can be excited. In the case of the quadrupole parameter, it excites the *x*-polarization incident light. Dipole and quadrupole are coupled (κ) to each other. Therefore, if a *y*-polarization incident light is incident, the quadrupole can excite due to the coupling effect. Fano resonance is applied to sensing by using high-Q factor and strong near field enhancement. Meanwhile, solving the differential equations by expressing the amplitudes of each state as $e^{j\omega t}$ can be derived as follows.

$$D = \frac{\{[j(\omega - \omega_Q) + r_Q]\alpha_{D_x} + j\kappa\alpha_{Q_x}\}E_x + [j(\omega - \omega_Q) + r_Q]\alpha_{D_y} E_y}{[j(\omega - \omega_D) + r_D][j(\omega - \omega_Q) + r_Q] + \kappa^2}$$

$$Q = \frac{\{[j(\omega - \omega_D) + r_D]\alpha_{Q_x} + j\kappa\alpha_{D_x}\}E_x + j\kappa\alpha_{D_y} E_y}{[j(\omega - \omega_D) + r_D][j(\omega - \omega_Q) + r_Q] + \kappa^2}$$

Next, the reflectivity can be obtained by applying the reciprocity theorem[36].

$$r_{xx} = \frac{E_x^{out}}{E_x^{in}} = -\frac{\alpha_{D_x} D + \alpha_{Q_x} Q}{E_x^{in}} = -\frac{\alpha_{D_x}^2 [j(\omega - \omega_Q) + \tau_Q^{-1}] + \alpha_{Q_x}^2 [j(\omega - \omega_D) + \tau_D^{-1}] + 2\alpha_{D_x}\alpha_{Q_x} j\kappa}{[j(\omega - \omega_D) + \tau_D^{-1}][j(\omega - \omega_Q) + \tau_Q^{-1}] + \kappa^2}$$

$$r_{yy} = \frac{E_y^{out}}{E_y^{in}} = -\frac{\alpha_{D_y} D}{E_y^{in}} = -\frac{\alpha_{D_y}^2 \left[j(\omega - \omega_Q) + \tau_Q^{-1} \right]}{[j(\omega - \omega_D) + \tau_D^{-1}][j(\omega - \omega_Q) + \tau_Q^{-1}] + \kappa^2}$$

Equations were added by a substance called ODT to measure the detection performance. The ODT material forms a self-assembling monolayer layer in gold. The ODT molecule's calibration wavelength has symmetric and asymmetric vibration frequencies at 3509 nm and 3427 nm, respectively. Because the 3427nm is more strong vibration, the amplitude of 3427nm is denoted by M, and the wavelength of 3509nm is denoted by M`. Then two expressions are added as follows.

$$\frac{dD}{dt} = j\omega_D D - \gamma_D D + j\kappa_{DQ} Q + \alpha_{D_x} S_x^{in} + \alpha_{D_y} S_y^{in}$$

$$\frac{dQ}{dt} = j\omega_Q Q - \gamma_Q Q + j\kappa_{DQ} D + j\kappa_{QM} M + j\kappa_{QM`} M` + \alpha_{Q_x} S_x^{in}$$

$$\frac{dM}{dt} = j\omega_M M - \gamma_M M + j\kappa_{QM} Q$$

$$\frac{dM`}{dt} = j\omega_{M`} M` - \gamma_{M`} M` + j\kappa_{QM`} Q$$

Here, ω_M and $\omega_{M`}$ represent the respective vibration frequencies generated in the ODT, and $\gamma_M$ and $\gamma_{M`}$ denote the damping frequency in the ODT. Similarly, by expressing the amplitudes of each state as $e^{j\omega t}$, the differential equation can be solved as follows.

$$\begin{aligned} A &= j(\omega - \omega_D) + \gamma_D \\ B &= j(\omega - \omega_Q) + \gamma_Q \\ C &= j(\omega - \omega_M) + \gamma_M \\ \mathcal{D} &= j(\omega - \omega_{M`}) + \gamma_{M`} \end{aligned}$$

$$D = \frac{\left[\left(BC\mathcal{D} + \kappa_{QM}^2 \mathcal{D} + \kappa_{QM`}^2 C \right) \alpha_{D_x} + j\kappa_{DQ} C\mathcal{D} \alpha_{D_x} \right] E_x + \left( BC\mathcal{D} + \kappa_{QM}^2 \mathcal{D} + \kappa_{QM`}^2 C \right) \alpha_{D_y} E_x}{ABC\mathcal{D} + \kappa_{QM}^2 \mathcal{D} + \kappa_{QM`}^2 C + \kappa_{DQ}^2 C\mathcal{D}}$$

$$Q = \frac{\left(jk_{DQ} C\mathcal{D} \alpha_{D_x} + AC\mathcal{D} \alpha_{D_x} \right) E_x + jk_{DQ} C\mathcal{D} \alpha_y E_y}{A\left(BC\mathcal{D} + \kappa_{QM}^2 \mathcal{D} + \kappa_{QM`}^2 C \right) + \kappa_{DQ}^2 C\mathcal{D}}$$

Finally, the equation is as follows.

$$r_{xx} = \frac{E_x^{out}}{E_x^{in}} = -\frac{\alpha_{D_x} D + \alpha_{Q_x} Q}{E_x^{in}} =$$

$$- \frac{\alpha_{D_x}^2 \left(BC\mathcal{D} + \kappa_{QM}^2 \mathcal{D} + \kappa_{QM`}^2 C\right) + \alpha_{Q_x}^2 AC\mathcal{D} + 2\ \alpha_{D_x}\ \alpha_{Q_x}\ j\kappa_{DQ} C\mathcal{D}}{ABC\mathcal{D} + \kappa_{QM}^2 \mathcal{D} + \kappa_{QM`}^2 C + \kappa_{DQ}^2 C\mathcal{D}}$$

$$r_{yy} = \frac{E_y^{out}}{E_y^{in}} = -\frac{\alpha_{D_y} D}{E_x^{in}} = - \frac{\alpha_{D_y}^2 \left(BC\mathcal{D} + \kappa_{QM}^2 \mathcal{D} + \kappa_{QM`}^2 C\right)}{A\left(BC\mathcal{D} + \kappa_{QM}^2 \mathcal{D} + \kappa_{QM`}^2 C\right) + \kappa_{DQ}^2 C\mathcal{D}}$$

5.2 TCMT Modelling Result

Coupling constants of between ODT molecule and quadrupole was calculated through TCMT modeling as follows. First, the TCMT modeling constant was set at 680nm of the substrate sample. As the L increases, the resonance frequency was red shifted, and ω_Q and ω_D were increased accordingly. However, as shown in the figure, as L increases to 740nm and 800nm, it appears to be slightly deviated from TCMT modeling. Because of this, the coupling constant of the ODT molecule and the quadrupole was different from the actual value. Similarly, considering the frequency shift by Etch, TCMT was the best match at L = 740nm in Etch structure, and slightly deviated at L = 680nm and 800nm.

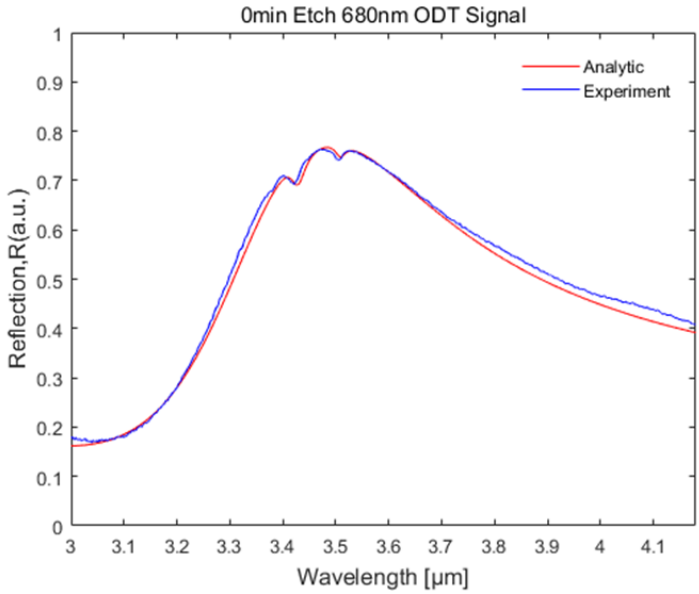

Figure 5-1. TCMT modelling to L = 680nm ODT coated experiment result with substrate structure

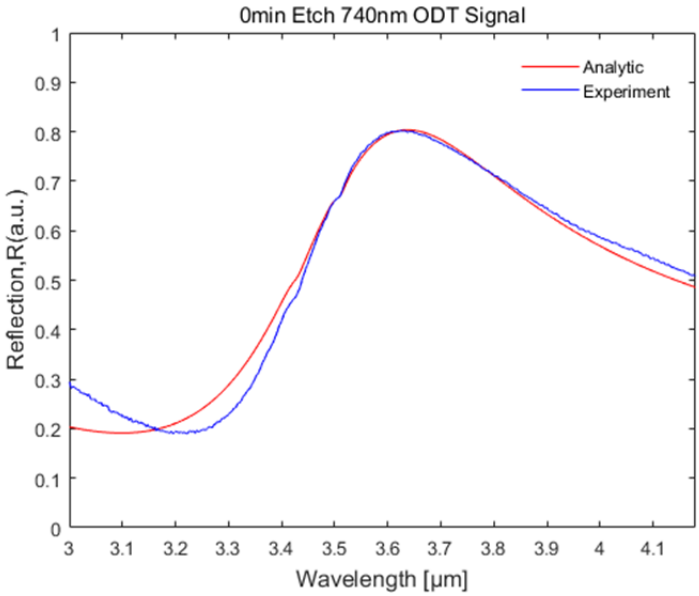

Figure 5-2. TCMT modelling to L = 740nm ODT coated experiment result with substrate structure

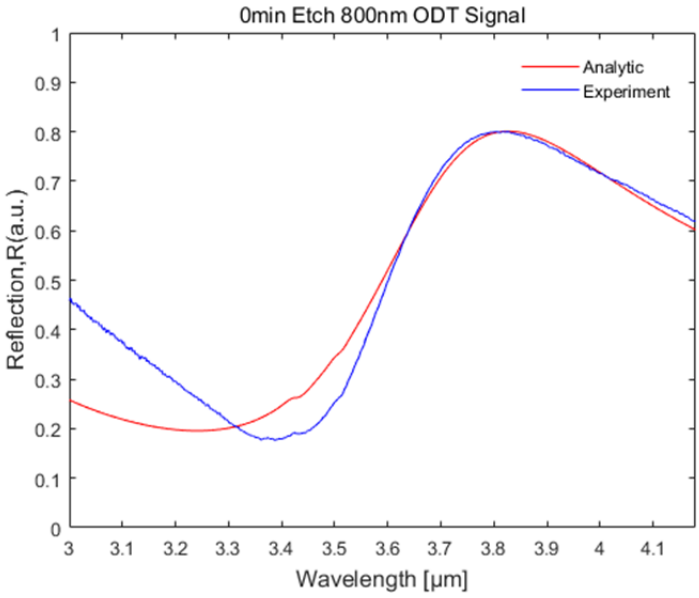

Figure 5-3. TCMT modelling to L = 800nm ODT coated experiment result with substrate structure

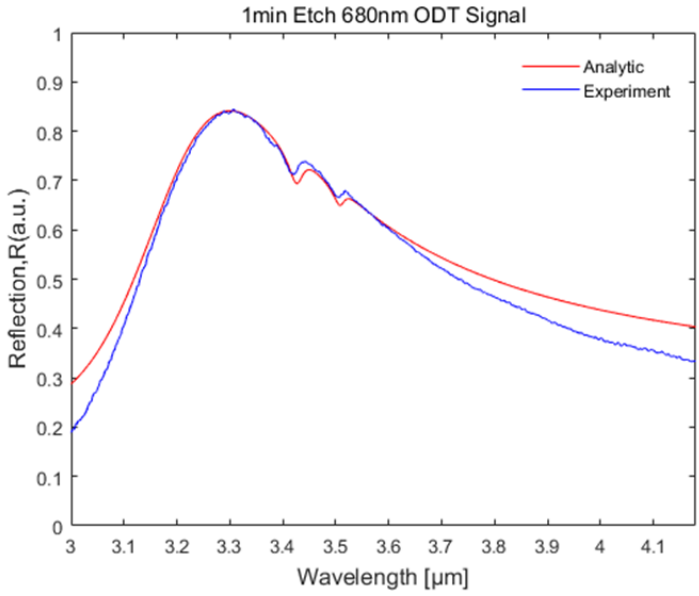

Figure 5-4. TCMT modelling to L = 680nm ODT coated experiment result with etch structure

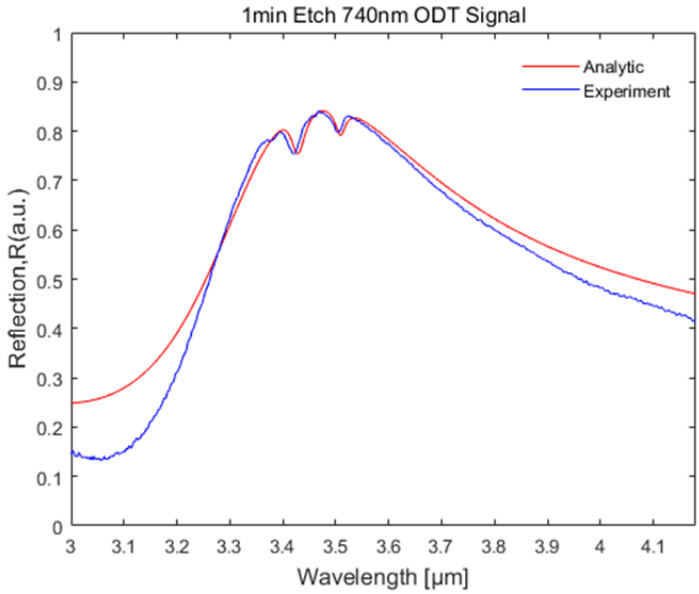

Figure 5-5. TCMT modelling to L = 740nm ODT coated experiment result with etch structure

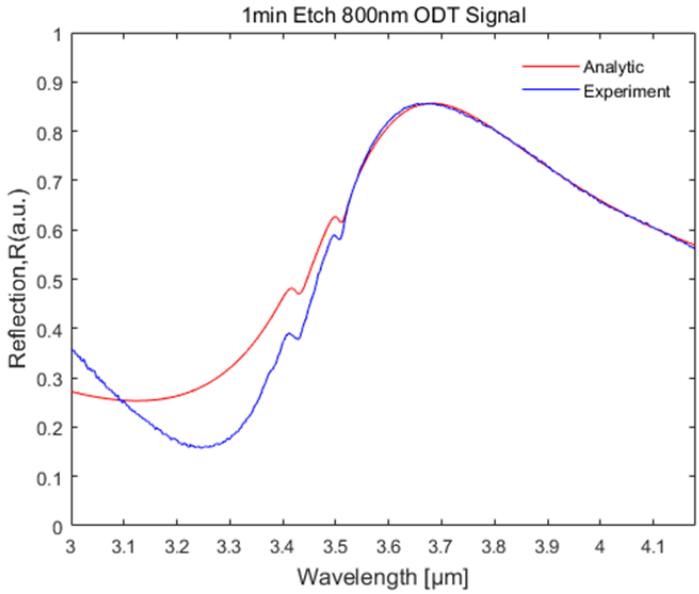

Figure 5-6. TCMT modelling to L = 800nm ODT coated experiment result with etch structure

[rad/s]	L=680nm	L=740nm	L=800nm
ω_Q	6.28×10^{14}	6.08×10^{14}	5.81×10^{14}

ω_D	7.65 x 10^{14}	7.4 x 10^{14}	7.07 x 10^{14}
ω_M	5.5 x 10^{14}	5.5 x 10^{14}	5.5 x 10^{14}
$\omega_{M`}$	5.37 x 10^{14}	5.37 x 10^{14}	5.37 x 10^{14}
κ_{DQ}	1.36 x 10^{14}	1.36 x 10^{14}	1.36 x 10^{14}
κ_{QM}	2.48 x 10^{12}	1.47 x 10^{12}	2.41 x 10^{12}
$\kappa_{QM`}$	1.61 x 10^{12}	1.23 x 10^{12}	1.23 x 10^{12}
γ_D	1.38 x 10^{14}	1.38 x 10^{14}	1.38 x 10^{14}
γ_Q	7.24 x 10^{12}	7.43 x 10^{12}	7.8 x 10^{12}
γ_M	2.45 x 10^{12}	2.45 x 10^{12}	2.45 x 10^{12}
$\gamma_{M`}$	1.8 x 10^{12}	1.8 x 10^{12}	1.8 x 10^{12}

Table 5-1. Fitting parameters of TCMT with substrate structure (0min Asher)

[rad/s]	L=680nm	L=740nm	L=800nm
ω_Q	6.57 x 10^{14}	6.3 x 10^{14}	6.03 x 10^{14}
ω_D	8.0 x 10^{14}	7.68 x 10^{14}	7.34 x 10^{14}
ω_M	5.5 x 10^{14}	5.5 x 10^{14}	5.5 x 10^{14}
$\omega_{M`}$	5.37 x 10^{14}	5.37 x 10^{14}	5.37 x 10^{14}
κ_{DQ}	1.36 x 10^{14}	1.36 x 10^{14}	1.36 x 10^{14}
κ_{QM}	4.21 x 10^{12}	3.36 x 10^{12}	3.36 x 10^{12}
$\kappa_{QM`}$	3.16 x 10^{12}	2.49 x 10^{12}	2.36 x 10^{12}

γ_D	1.38 x 10^{14}	1.38 x 10^{14}	1.38 x 10^{14}
γ_Q	7.24 x 10^{12}	7.43 x 10^{12}	7.8 x 10^{12}
γ_M	2.45 x 10^{12}	2.45 x 10^{12}	2.45 x 10^{12}
$\gamma_{M`}$	1.8 x 10^{12}	1.8 x 10^{12}	1.8 x 10^{12}

Table 5-2. Fitting parameters of TCMT with etch structure (1min Asher)

VI. Conclusion

6.1 Conclusion

In conclusion, nanopedestal Fano metamaterials was designed and demonstrated for ultra-sensitive detection and characterization of molecules showing high Q-factor existing strong coupling between Fano resonance mode and molecular absorption mode. The undercut effect was taken under gold rods using Asher equipment on quartz substrate. This was expected to increase the SEIRA detection signal due to an increase in the sensing area.

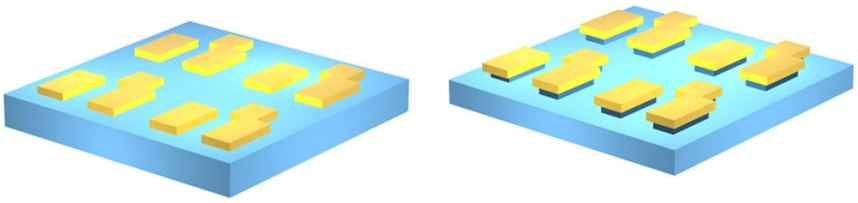

Figure 6-1. Substrate sample (left) and Etch sample (right) by Asher process

Considering the blue shift of resonance peak due to the reduction of effective refractive index by undercut method, to set Fano resonance frequency to ODT's CH_2 absorption frequency, gold rod's length was made by L = 680nm, 740nm, 800nm. (See Figure 4-2). Simulation model was introduced by Lumerical FDTD to check Fano structure's quadrupole and dipole resonance frequency. In the experiment result, substrate sample (L = 680nm) (0min Asher process) and etch sample (L=740nm) (1min Asher process)'s quadrupole resonance frequency was fixed to ODT's absorption frequency. The ODT signal result spectrum was modeled through TCMT. As a result, κ_{QM} increased by 1.35 times and $\kappa_{QM`}$ increased by 1.55 times due to etch undercut effect.

Case	κ_{QM} [3.427um]	$\kappa_{QM`}$ [3.509um]
Substrate L=680nm	2.48 x 10^{12} rad/s	1.61 x 10^{12} rad/s
Etch L=740nm	3.36 x 10^{12} rad/s	2.49 x 10^{12} rad/s

Table 6-1. Extracted coupling constant between quadrupole mode and molecular absorption mode

The cause of increase of detection signal was increased sensing area and field enhancement. So, to measure performance, the integrated field intensity was calculated using a Lumerical simulation, resulting in a 1.37-fold increase.

Case	Sensing Area [μm^2]	Integrated Near-field Intensity $\int_0^{V_{ODT}} \frac{I}{I_0} dV$ [10^9 x nm^3]
Substrate L=680nm	1.22	3.76
Etch L=740nm	1.47	5.16

Table 6-2. Calculated and simulated sensing area, integrated near-field intensity

6.2 Outlook

This concept of nanopedestal Fano resonance that features enhanced filed profile and added contact area can be applied in extremely low detection signal. However, due to the asymmetric spectrum characteristic, the peak to peak is lower than that of the lorentzian type spectrum, which is the dipole resonance. To compensate for this, a plasmonic Fano structure with an MIM absorber structure can be made. And by changing the recipe conditions of the NIL process, the gap between the Fano structures can be reduced from 200nm to 100nm to maximize the coupling effect. Moreover, this structure has many more elements to optimize like coupling between dipole and quadrupole mode. Therefore, strong electric field enhancement enables the application of metalens and 3D holograms which need extremely distorted electric field path.

REFERENCES

(1) Engheta, N.; Ziolkowski, R. W., *Metamaterials: physics and engineering explorations*. John Wiley & Sons: 2006.

(2) http://cobweb.ecn.purdue.edu/~ece695s/

(3) Zayats, A. V.; Smolyaninov, I. I.; Maradudin, A. A. J. P. r., Nano-optics of surface plasmon polaritons. **2005,** *408* (3-4), 131-314.

(4) Barnes, W. L.; Murray, W. A.; Dintinger, J.; Devaux, E.; Ebbesen, T. W., Surface plasmon polaritons and their role in the enhanced transmission of light through periodic arrays of subwavelength holes in a metal film. *Phys Rev Lett* **2004,** *92* (10), 107401.

(5) Zayats, A. V.; Smolyaninov, I. I. J. J. o. O. A. P.; Optics, A., Near-field photonics: surface plasmon polaritons and localized surface plasmons. **2003,** *5* (4), S16.

(6) Mayer, K. M.; Hafner, J. H., Localized surface plasmon resonance sensors. *Chem Rev* **2011,** *111* (6), 3828-57.

(7) Chen, B.; Meinertzhagen, I. A.; Shaw, S. R., Circadian rhythms in light-evoked responses of the fly's compound eye, and the effects of neuromodulators 5-HT and the peptide PDF. *J Comp Physiol A* **1999,** *185* (5), 393-404.

(8) Willets, K. A.; Van Duyne, R. P., Localized surface plasmon resonance spectroscopy and sensing. *Annu Rev Phys Chem* **2007,** *58*, 267-97.

(9) Ozbay, E., Plasmonics: merging photonics and electronics at nanoscale dimensions. *Science* **2006,** *311* (5758), 189-93.

(10) Atwater, H. A. J. S. A., The promise of plasmonics. **2007,** *296* (4), 56-62.

(11) Brongersma, M. L.; Shalaev, V. M., Applied physics. The case for plasmonics. *Science* **2010,** *328* (5977), 440-1.

(12) Ayata, M.; Fedoryshyn, Y.; Heni, W.; Baeuerle, B.; Josten, A.; Zahner, M.; Koch, U.; Salamin, Y.; Hoessbacher, C.; Haffner, C. J. S., High-speed plasmonic modulator in a single metal layer. **2017,** *358* (6363), 630-632.

(13) Shalaev, V. M.; Cai, W.; Chettiar, U. K.; Yuan, H.-K.; Sarychev, A. K.; Drachev, V. P.; Kildishev, A. V. J. O. l., Negative index of refraction in optical metamaterials. **2005,** *30* (24), 3356-3358.

(14) Sassi, R.; Bond, R. R.; Cairns, A.; Finlay, D. D.; Guldenring, D.; Libretti, G.; Isola, L.; Vaglio, M.; Poeta, R.; Campana, M.; Cuccia, C.; Badilini, F., PDF-ECG in clinical practice: A model for long-term preservation of digital 12-lead ECG data. *J Electrocardiol* **2017,** *50* (6), 776-780.

(15) Shelby, R. A.; Smith, D. R.; Schultz, S., Experimental verification of a negative index of refraction. *Science* **2001,** *292* (5514), 77-9.

(16) Fang, N.; Lee, H.; Sun, C.; Zhang, X., Sub-diffraction-limited optical imaging with a silver superlens. *Science* **2005,** *308* (5721), 534-7.

(17) Liu, Z.; Lee, H.; Xiong, Y.; Sun, C.; Zhang, X., Far-field optical hyperlens magnifying sub-diffraction-limited objects. *Science* **2007,** *315* (5819), 1686.

(18) Zhang, X.; Liu, Z., Superlenses to overcome the diffraction limit. *Nat Mater* **2008,** *7* (6), 435-41.

(19) Smith, D. R.; Pendry, J. B.; Wiltshire, M. C., Metamaterials and negative refractive index. *Science* **2004,** *305* (5685), 788-92.

(20) Pendry, J. B., Negative refraction makes a perfect lens. *Phys Rev Lett* **2000,** *85* (18), 3966-9.

(21) Adato, R.; Yanik, A. A.; Amsden, J. J.; Kaplan, D. L.; Omenetto, F. G.; Hong, M. K.; Erramilli, S.; Altug, H., Ultra-sensitive vibrational spectroscopy of protein monolayers with plasmonic nanoantenna arrays. *Proc Natl Acad Sci U S A* **2009,** *106* (46), 19227-32.

(22) Liu, N.; Mesch, M.; Weiss, T.; Hentschel, M.; Giessen, H., Infrared perfect absorber and its application as plasmonic sensor. *Nano Lett* **2010,** *10* (7), 2342-8.

(23) Kabashin, A. V.; Evans, P.; Pastkovsky, S.; Hendren, W.; Wurtz, G. A.; Atkinson, R.; Pollard, R.; Podolskiy, V. A.; Zayats, A. V., Plasmonic nanorod metamaterials for biosensing. *Nat Mater* **2009,** *8* (11), 867-71.

(24) Lassiter, J. B.; Sobhani, H.; Fan, J. A.; Kundu, J.; Capasso, F.; Nordlander, P.; Halas, N. J., Fano resonances in plasmonic nanoclusters: geometrical and chemical tunability. *Nano Lett* **2010,** *10* (8), 3184-9.

(25) Meier, R. In Handbook of Vibrational Spectroscopy; Chalmers, J.,Griffiths, P. R., Eds.; John Wiley & Sons Ltd.: Chichester, UK, **2003**.

(26) Neubrech, F.; Huck, C.; Weber, K.; Pucci, A.; Giessen, H., Surface-Enhanced Infrared Spectroscopy Using Resonant Nanoantennas. *Chem Rev* **2017**.

(27) Stuart, B. H. Spectral Analysis; John Wiley & Sons Ltd.: Chichester, UK, **2005**.

(28) Fano, U. J. P. R., Effects of configuration interaction on intensities and phase shifts. **1961,** *124* (6), 1866.

(29) Miroshnichenko, A. E.; Flach, S.; Kivshar, Y. S. J. R. o. M. P., Fano resonances in nanoscale structures. **2010,** *82* (3), 2257.

(30) Fedotov, V. A.; Rose, M.; Prosvirnin, S. L.; Papasimakis, N.; Zheludev, N. I., Sharp trapped-mode resonances in planar metamaterials with a broken structural symmetry. *Phys Rev Lett* **2007,** *99* (14), 147401.

(31) Wu, C.; Khanikaev, A. B.; Shvets, G., Broadband slow light metamaterial based on a double-continuum Fano resonance. *Phys Rev Lett* **2011,** *106* (10), 107403.

(32) Wu, C.; Khanikaev, A. B.; Adato, R.; Arju, N.; Yanik, A. A.; Altug, H.; Shvets, G., Fano-resonant asymmetric metamaterials for ultrasensitive spectroscopy and identification of molecular monolayers. *Nat Mater* **2011,** *11* (1), 69-75.

(33) Cetin, A. E.; Etezadi, D.; Altug, H. J. A. O. M., Accessible nearfields by nanoantennas on nanopedestals for ultrasensitive vibrational spectroscopy. **2014,** *2* (9), 866-872.

(34) Kalantzopoulos, G. N.; Lundvall, F.; Checchia, S.; Lind, A.; Wragg, D. S.; Fjellvag, H.; Arstad, B., In Situ Flow MAS NMR Spectroscopy and Synchrotron PDF Analyses of the Local Response of the Bronsted Acidic Site in SAPO-34 during Hydration at Elevated Temperatures. *Chemphyschem* **2018,** *19* (4), 519-528.

(35) Haus, H. A., *Waves and fields in optoelectronics*. Prentice-Hall: 1984.

(36) Ruan, Z.; Fan, S. J. T. J. o. P. C. C., Temporal coupled-mode theory for Fano resonance in light scattering by a single obstacle. **2009,** *114* (16), 7324-7329.

감사의 글

3년의 시간 동안 끝까지 저를 지도해주신 이종원 지도 교수님께 감사의 말씀을 전합니다. 인내심을 가지고 지도해주심 덕분에 이렇게 졸업합니다.

그리고 기계연구원에서 1년 동안 지도해주신 정주연 박사님께도 감사의 말씀을 전합니다. 바쁘신 와중에도 친절히 저를 가르쳐 주시고 도와주셔서 많이 배울 수 있었습니다.

그 동안 어떤 곳 보다 가장 많은 시간을 보냈던 NPDL 연구실도 저에게 소중한 기억으로 남았습니다. 재밌었던 인용이형, 다재다능했던 재연이 그리고 대익이, 성진이, 형주, 민균이, 동례 모두 건강하고 행복하길 바랍니다.

1년 간의 짧은 기계연구원 생활 동안에도 따뜻하게 대하여 주셔서 잘 적응 할 수 있었습니다. 정준호 본부장님, 최대근 박사님, 이지혜 박사님, 최준혁 박사님, 전소희 박사님, 황순형 박사님, 강혁중 연구원님, 조지준 박사님, 복문정 박사님, 강혁준 연구원님, 이호영 연구원님, 고지우 연구원님, 안준성 연구원님, 정용록 연구원님, 김정민 연구원님 모두 감사드립니다.

끝으로 방황하는 저를 끝까지 포기하지 않고 사랑과 관심을 주신 부모님에게 감사 드립니다.

2019.12.20

정용석